

2D Numerical Study of Nonlinear Magnetic Reconnection

Dingyun Liu

APC523 2022 Spring

1 Introduction

Magnetic reconnection is the topological rearrangement of magnetic field lines, which commonly takes place in magnetized astrophysical and laboratory plasmas. Accompanied by the rearrangement of macroscopic plasma quantities such as mass and energy, it is a mechanism of great interest.

Magnetic reconnection plays an important role in various physical systems. Here are two examples. In ideal MHD, the plasma is frozen to the magnetic field lines, which makes it impossible for the plasma embedded on the incoming solar wind lines to penetrate the earth's magnetosphere. However, the finite plasma conductivity leads to magnetic reconnection. Some of the solar-wind lines can break and reattach to lines in the magnetosphere, allowing the plasma to penetrate and eventually detected from the earth. The other example is the self-reorganization process in current carrying fusion plasmas. The topology change of a set of field lines leads to a new equilibrium with lower magnetic energy. In tokamaks, particularly, it is characterized by cycles of ramping up and sudden drop of core electron density and temperature, which may lead to disruptions.

Both of the two examples are characterized by high Lundquist number S . According to Sweet-Parker's model, $\tau_{SP} \propto S^{1/2}$, the reconnection time can be very long, much longer than that observed in space or in tokamaks. So it is not possible to realize fast reconnection at high S within the frame of resistive MHD. However, A. Bhattacharjee and Y. Huang studied nonlinear evolution of reconnection in large systems (thin current sheet $\delta_{SP}/L \ll 1$). Over a critical S , the current sheet becomes unstable to plasmoid instability (a super-Alfvénic tearing instability). Its reconnection rate only depends weakly on S , and larger than the Sweet-Parker rate by nearly an order of magnitude. [1]

2 Mathematical Model

The magnetic field is represented as

$$\mathbf{B} = \nabla\psi(x, z) \times \hat{y} \quad (1)$$

where ψ is the flux function and the y component of the scalar potential. The relevant dynamical equations are given by

$$\frac{\partial \rho}{\partial t} + \nabla \cdot (\rho \mathbf{v}) = 0 \quad (2a)$$

$$\frac{\partial \rho \mathbf{v}}{\partial t} + \nabla \cdot (\rho \mathbf{v} \mathbf{v}) = -\nabla p - \nabla \psi \nabla^2 \psi \quad (2b)$$

$$\mathbf{E} + \mathbf{v} \times \mathbf{B} = \eta \mathbf{J} \quad (2c)$$

The scalar potential p is assumed to observe isothermal equation of state

$$p = 2\rho T \quad (3)$$

where T is a constant temperature. Subtract Eq. 7a \mathbf{v} from Eq. 2b, then second equation of the set becomes

$$\frac{\partial \mathbf{v}}{\partial t} + (\mathbf{v} \cdot \nabla) \mathbf{v} = -2T \frac{\nabla \rho}{\rho} - \frac{1}{\rho} \nabla \psi \nabla^2 \psi \quad (4)$$

According to Faraday's law

$$\nabla \times \mathbf{E} = -\frac{\partial \mathbf{B}}{\partial t} \quad (5)$$

so the Eq. 2c becomes

$$\frac{\partial \psi}{\partial t} + \mathbf{v} \cdot \nabla \psi = \eta \nabla^2 \psi \quad (6)$$

Eventually, the equations we are going to numericalize look like

$$\frac{\partial \rho}{\partial t} + \nabla \cdot (\rho \mathbf{v}) = 0 \quad (7a)$$

$$\frac{\partial \mathbf{v}}{\partial t} + (\mathbf{v} \cdot \nabla) \mathbf{v} = -2T \frac{\nabla \rho}{\rho} - \frac{1}{\rho} \nabla \psi \nabla^2 \psi \quad (7b)$$

$$\frac{\partial \psi}{\partial t} + \mathbf{v} \cdot \nabla \psi = \eta \nabla^2 \psi \quad (7c)$$

3 Proposed Work

The original work by Bhattacharjee and Huang gave a 2D numerical solution to this problem. A variable mesh is applied to resolve the sharp spatial gradient in the current layer. Spatial derivatives are evaluated to fourth order with a five-point stencil in the finite difference scheme, and the time derivatives are evaluated to second order in a leapfrog trapezoidal scheme.

To reproduce this work, first we are going to apply the same algorithm simplified by uniform mesh. If this proves to work, then we will try symplectic Euler scheme to compare the accuracy and a non-symplectic RK4 to compare different behaviors in phase-space volume.

4 Problem Statement

4.1 Equations

With only variations in the $x - z$ plane, $\partial/\partial y = 0$. Eq. 7 becomes

$$\frac{\partial \rho}{\partial t} = -\rho \left(\frac{\partial v_x}{\partial x} + \frac{\partial v_z}{\partial z} \right) - \left(v_x \frac{\partial \rho}{\partial x} + v_z \frac{\partial \rho}{\partial z} \right) = f_\rho(\rho, v_x, v_z) \quad (8a)$$

$$\frac{\partial v_x}{\partial t} = - \left(v_x \frac{\partial v_x}{\partial x} + v_z \frac{\partial v_x}{\partial z} \right) - \frac{2T}{\rho} \frac{\partial \rho}{\partial x} - \frac{1}{\rho} \frac{\partial \psi}{\partial x} \left(\frac{\partial^2 \psi}{\partial x^2} + \frac{\partial^2 \psi}{\partial z^2} \right) = f_{v_x}(\rho, v_x, v_z, \psi) \quad (8b)$$

$$\frac{\partial v_z}{\partial t} = - \left(v_x \frac{\partial v_z}{\partial x} + v_z \frac{\partial v_z}{\partial z} \right) - \frac{2T}{\rho} \frac{\partial \rho}{\partial z} - \frac{1}{\rho} \frac{\partial \psi}{\partial z} \left(\frac{\partial^2 \psi}{\partial x^2} + \frac{\partial^2 \psi}{\partial z^2} \right) = f_{v_z}(\rho, v_x, v_z, \psi) \quad (8c)$$

$$\frac{\partial \psi}{\partial t} = - \left(v_x \frac{\partial \psi}{\partial x} + v_z \frac{\partial \psi}{\partial z} \right) + \eta \left(\frac{\partial^2 \psi}{\partial x^2} + \frac{\partial^2 \psi}{\partial z^2} \right) = f_\psi(\rho, v_x, v_z, \psi) \quad (8d)$$

To realize 4th-order accuracy in space, we apply the 5-point central scheme for the time derivatives

$$g'(x_i) = \frac{-f_{i+2} + 8f_{i+1} - 8f_{i-1} + f_{i-2}}{12h} \quad (9a)$$

$$g^{(2)}(x_i) = \frac{-f_{i+2} + 16f_{i+1} - 30f_i + 16f_{i-1} - f_{i-2}}{12h^2} \quad (9b)$$

Take the derivatives of ψ for example

$$\frac{\partial \psi_{i,j}}{\partial x} = \frac{-\psi_{i+2,j} + 8\psi_{i+1,j} - 8\psi_{i-1,j} + \psi_{i-2,j}}{12\Delta x} \quad (10a)$$

$$\frac{\partial \psi_{i,j}}{\partial z} = \frac{-\psi_{i,j+2} + 8\psi_{i,j+1} - 8\psi_{i,j-1} + \psi_{i,j-2}}{12\Delta z} \quad (10b)$$

$$\frac{\partial^2 \psi_{i,j}}{\partial x^2} = \frac{-\psi_{i+2,j} + 16\psi_{i+1,j} - 30\psi_{i,j} + 16\psi_{i-1,j} - \psi_{i-2,j}}{12\Delta x^2} \quad (10c)$$

$$\frac{\partial^2 \psi_{i,j}}{\partial z^2} = \frac{-\psi_{i,j+2} + 16\psi_{i,j+1} - 30\psi_{i,j} + 16\psi_{i,j-1} - \psi_{i,j-2}}{12\Delta z^2} \quad (10d)$$

The 2nd-order leap-frog trapezoidal scheme in time is given by

$$\begin{aligned} kick : v_x^{n+1/2} &= v_x^n + f_{v_x}(\rho^n, v_x^n, v_z^n, \psi^n) \frac{\Delta t}{2} \\ v_z^{n+1/2} &= v_z^n + f_{v_z}(\rho^n, v_x^n, v_z^n, \psi^n) \frac{\Delta t}{2} \\ drift : \rho^{n+1} &= \rho^n + f_\rho(\rho^n, v_x^{n+1/2}, v_z^{n+1/2}) \Delta t \\ \psi^{n+1} &= \psi^n + f_\psi(\rho^n, v_x^{n+1/2}, v_z^{n+1/2}, \psi^n) \Delta t \\ kick : v_x^{n+1} &= v_x^{n+1/2} + f_{v_x}(\rho^{n+1}, v_x^{n+1/2}, v_z^{n+1/2}, \psi^{n+1}) \frac{\Delta t}{2} \\ v_z^{n+1} &= v_z^{n+1/2} + f_{v_z}(\rho^{n+1}, v_x^{n+1/2}, v_z^{n+1/2}, \psi^{n+1}) \frac{\Delta t}{2} \end{aligned} \quad (11)$$

4.2 Initial conditions

The process begins with four flux tubes, which are unstable to the coalescence instability. The initial equilibrium is given by

$$\psi = A_0 \sin(2\pi x/L) \sin(2\pi z/L) \quad (12)$$

where $L = \sqrt{2}$ and $A_0 = L/\sqrt{2}\pi$. The density field is uniformly 1 at the beginning, so the pressure is approximately 6 give that $T = 3$. And the fluid velocity $\mathbf{v}(t=0) = (v_x, v_z) = (0, 0)$.

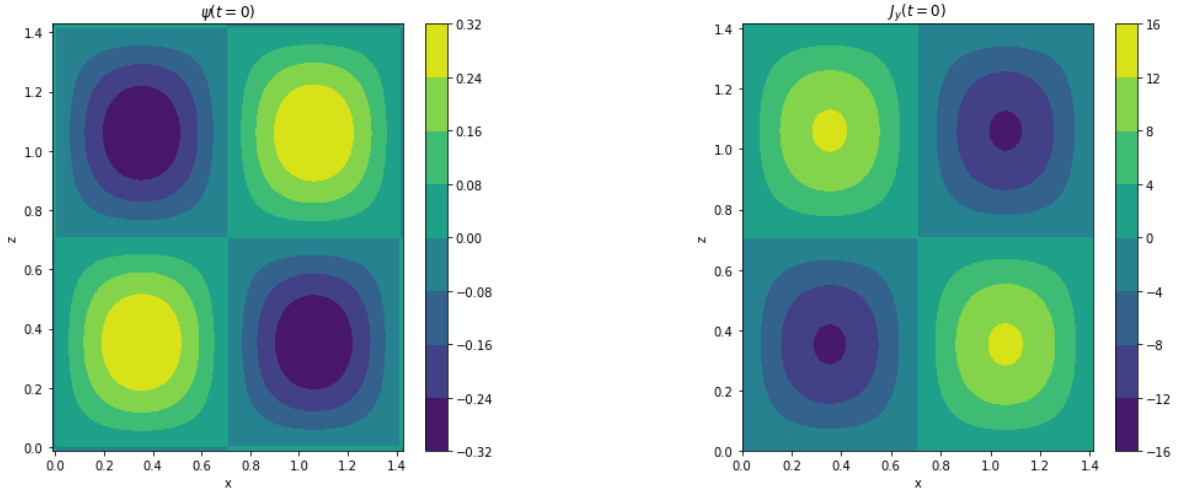


Figure 1: Flux function ψ and y component of current density J_y at the initial equilibrium.

4.3 Boundary conditions

The 2D geometry is doubly periodic, so we have double-periodic ρ , v_x , v_z , and ψ . With five-point stencil difference scheme, 2 layers of ghost cells are applied to each boundary.

5 Numerical Results

The simulation region is $[0, \sqrt{2}] \times [0, \sqrt{2}]$ on the $x - z$ plane. For the sake of simplicity, uniform mesh with 201×201 grid points is applied here.

5.1 Leap-frog scheme

It had been intended to simulate the 3s at the beginning to see the development of the plasmoid instability. So the whole period $T = 3$, and $dt = 0.001$. However, strong oscillations appeared near the $z = 0$ and $z = \sqrt{2}$ boundaries, and the fields blew up rapidly. The density field went negative at the 157th step. Below are results at the 150th time step.

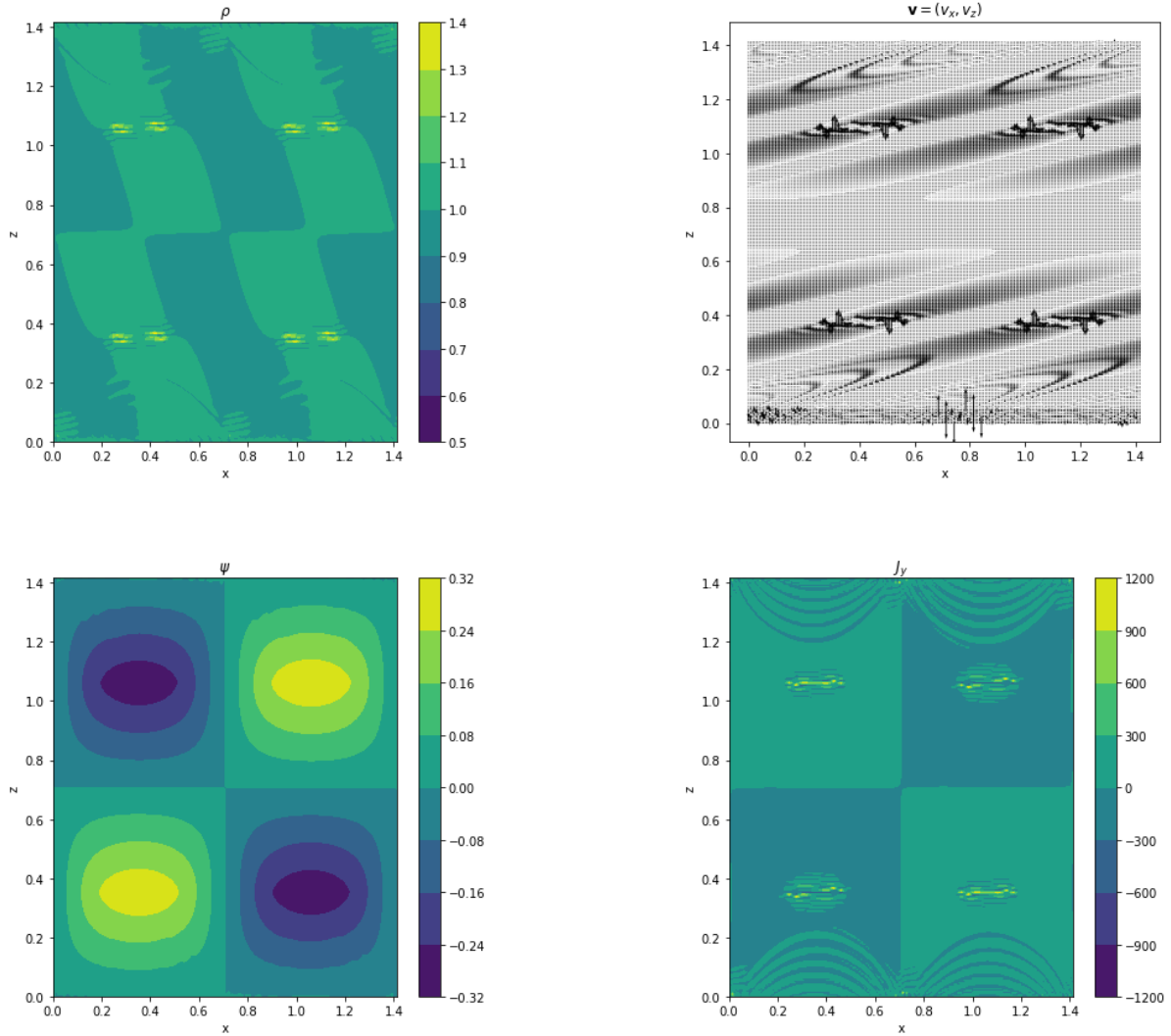


Figure 2: Density ρ , velocity \mathbf{v} , flux function ψ , and y component of current density J_y at $t = 0.15$.

With Ampère's law

$$\mathbf{J} = \nabla \times \mathbf{B} \quad (13)$$

The y component of current density J_y can be derived from the flux function ψ

$$J_y = \frac{\partial B_z}{\partial x} - \frac{\partial B_x}{\partial z} = \frac{\partial^2 \psi}{\partial x^2} + \frac{\partial^2 \psi}{\partial z^2} \quad (14)$$

The density is not uniform anymore, and some peaks appeared in each flux tube. As is shown in the upper right plot, the velocity field is highly stratified. The contour of J_y (lower right plot) shows that current sheets have been formed in each flux tube, but we can't see any plasmoid instability developing yet.

5.2 Symplectic Euler scheme

The density peaks and current sheets in each flux tube. The results are less influenced by the dramatic oscillations on the boundaries. A similar problem is that the field blew up rapidly and density field went negative at the 147th step. Below are results at the 140th time step.

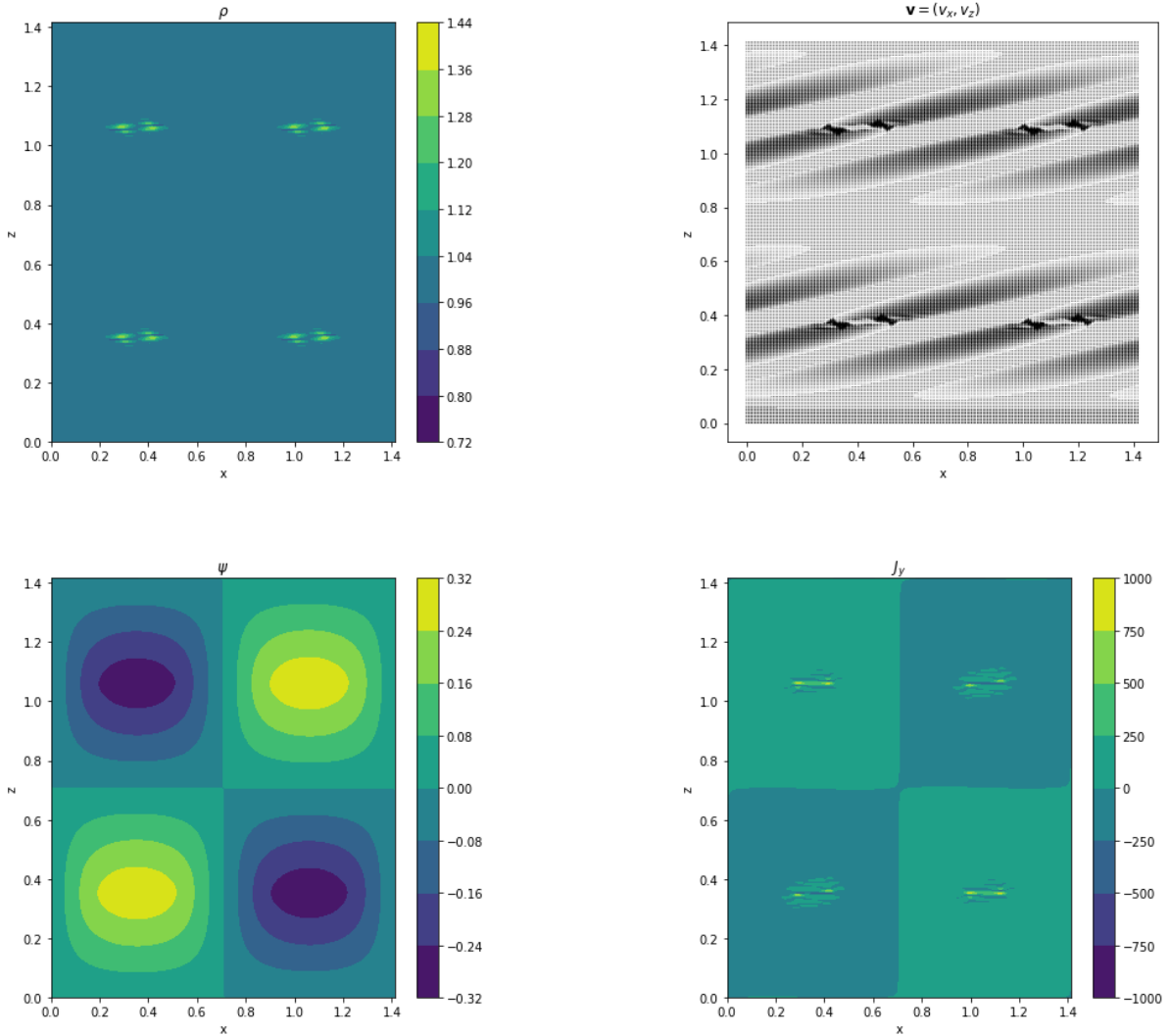


Figure 3: Density ρ , velocity \mathbf{v} , flux function ψ , and y component of current density J_y at $t = 0.15$.

6 Problems at the Boundary

Large oscillations happened at the boundary in the leap-frog scheme. The amplitude of $\frac{\partial v_x}{\partial x}$ and $\frac{\partial v_z}{\partial z}$ blows up first at the $z = 0$ and $z = \sqrt{2}$ boundaries and then at the $x = 0$ and $x = \sqrt{2}$, which drives the local ρ negative.

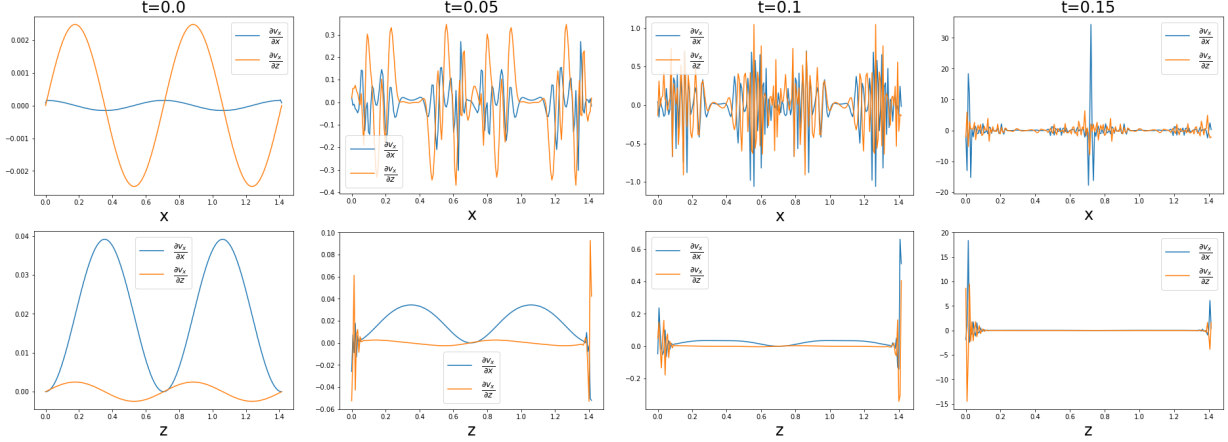


Figure 4: Cross sections of $\partial v_x/\partial x$ (blue curve) and $\partial v_z/\partial z$ (orange curve) on the $z = 0$ (top) and $x = 0$ (bottom) boundaries at $t = 0.0, 0.05, 0.10, 0.15$ in the leap-frog scheme.

This is not expected for doubly periodic boundary conditions. After checking the setting of boundary conditions, we try to expand the simulation region to $[0, 3\sqrt{2}] \times [0, 3\sqrt{2}]$ so that the original boundaries are surrounded by other flux tubes. There are no more expected oscillations there. The partial derivatives still blow up, but they become periodic, and the oscillation amplitude gets smaller at the same instance. The influence of the boundaries decreases with the expansion of simulation region.

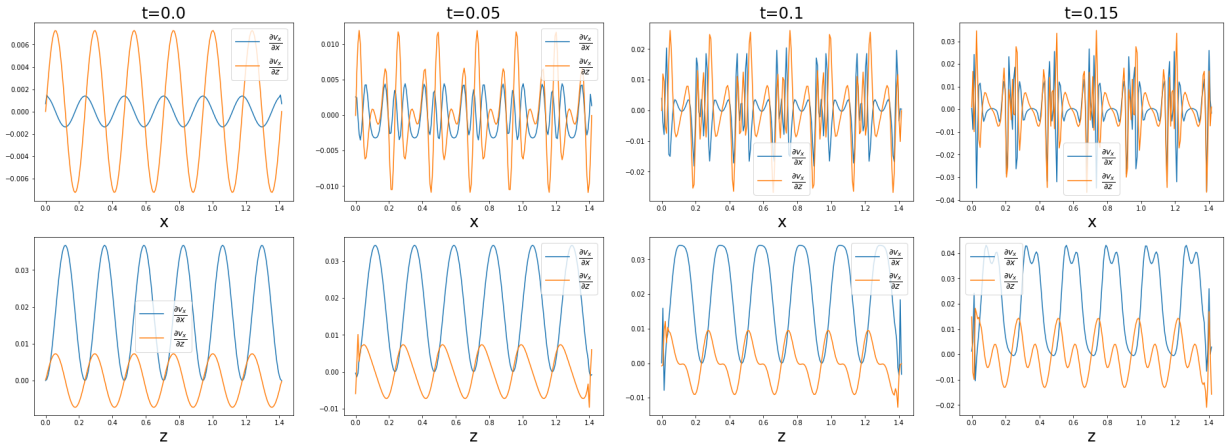


Figure 5: Cross sections of $\partial v_x/\partial x$ (blue curve) and $\partial v_z/\partial z$ (orange curve) on the $z = 0$ (top) and $x = 0$ (bottom) boundaries at $t = 0.0, 0.05, 0.10, 0.15$ after expanding the simulation region.

The boundary is less of a problem in the symplectic Euler scheme. The boundaries in x direction look good, with only small wiggles on the one end of the boundaries in z direction.

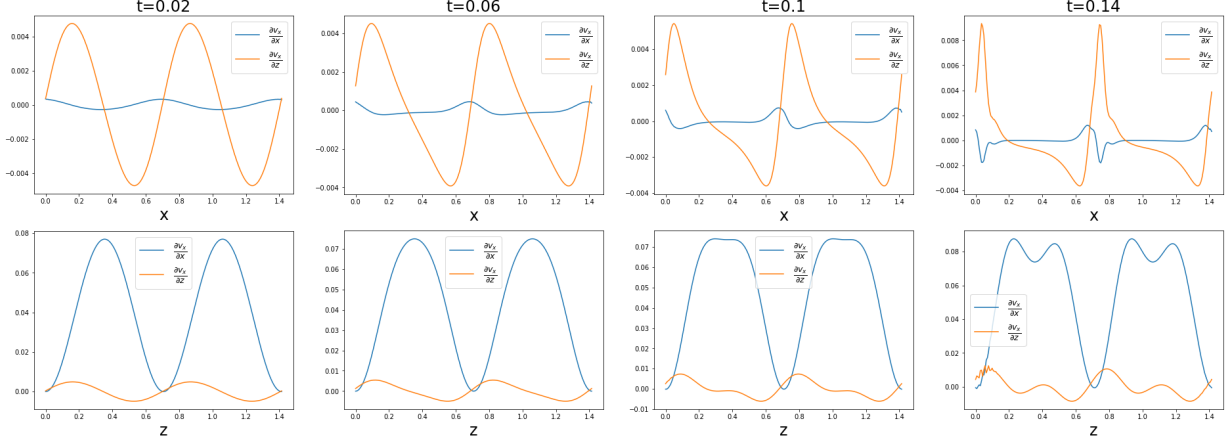


Figure 6: Cross sections of $\partial v_x/\partial x$ (blue curve) and $\partial v_z/\partial z$ (orange curve) on the $z = 0$ (top) and $x = 0$ (bottom) boundaries at $t = 0.02, 0.06, 0.10, 0.14$ in the symplectic Euler scheme.

7 Summary

In this project, attempts have been made to reproduce previous work with simplification. The leap-frog scheme was a commonly used in MHD simulations due to its conservation of phase-space, which is an essential property in physics. Here we applied another symplectic scheme, the symplectic Euler for a comparison. It had better behavior at the boundaries in this simulation. However, the code needs further elaboration to keep the fields from blowing up.

References

- [1] A. Bhattacharjee et al. “Fast reconnection in high-Lundquist-number plasmas due to the plasmoid Instability”. In: *Physics of Plasmas* 16.11 (2009), p. 112102. DOI: 10.1063/1.3264103. eprint: <https://doi.org/10.1063/1.3264103>. URL: <https://doi.org/10.1063/1.3264103>.